

# Guidelines for designing 2D and 3D plasmonic stub resonators

SOLMAZ NAGHIZADEH<sup>1</sup> AND ŞÜKRÜ EKIN KOCABAŞ<sup>2,\*</sup>

<sup>1</sup>Department of Physics, Koç University, Istanbul 34450, Turkey

<sup>2</sup>Department of Electrical and Electronics Engineering, Koç University, Istanbul 34450, Turkey

\*Corresponding author: ekocabas@ku.edu.tr

Received 13 October 2016; revised 27 November 2016; accepted 28 November 2016; posted 28 November 2016 (Doc. ID 278584); published 22 December 2016

**In this work, we compare the performance of plasmonic waveguide integrated stub resonators based on 2D metal-dielectric-metal and 3D slot waveguide (SWG) geometries. We show that scattering matrix theory can be extended to 3D devices, and by employing scattering matrix theory, we provide the guidelines for designing plasmonic 2D and 3D single-stub and double-stub resonators with a desired spectral response at the design wavelength. We provide transmission maps of 2D and 3D double-stub resonators versus stub lengths, and we specify the different regions on these maps that result in a minimum, a maximum, or a plasmonically induced transparency shape in the transmission spectrum. Radiation loss from waveguide terminations leads to a degradation of the 3D SWG-based resonators. We illustrate improved waveguide terminations that boost resonator properties. We verify our results with 3D finite-difference time-domain (FDTD) simulations.** © 2016 Optical Society of America

**OCIS codes:** (250.5403) Plasmonics; (140.4780) Optical resonators; (130.7408) Wavelength filtering devices; (270.0270) Quantum optics; (280.4788) Optical sensing and sensors.

<https://doi.org/10.1364/JOSAB.34.000207>

## 1. INTRODUCTION

Surface plasmon polaritons (SPPs) are one-dimensional bound electromagnetic waves propagating along metal-dielectric (MD) interfaces. These nonradiative modes result from longitudinal oscillation of free electrons along MD interfaces that are excited by an incident electromagnetic wave with its propagation vector modified by a prism or a grating to match the propagation vector of an SPP mode [1]. The coupling of free electrons with the incident electromagnetic wave assists the wave to propagate along metallic surfaces much further than the skin depth of the bulk metal. SPP modes exponentially decay into the dielectric and metallic media on both sides of the MD interface. This is the origin of the subwavelength confinement in the plasmonic field, and more confinement can be reached by bringing two MD layers together [2]. Plasmonic devices based on SPP modes are therefore capable of overcoming the diffraction limit, which dictates the minimum size of the photonic devices. Many waveguide structures have been proposed and have been investigated for SPP waves [3–9]. Among them, 2D metal-dielectric-metal (MDM) plasmonic waveguides [2] with confinement in one dimension, and 3D plasmonic slot waveguides (SWGs) [7,8] with confinement in two dimensions have gained popularity due to their high confinement, relatively long propagation length, wide bandwidth, and ease of fabrication.

The development of resonators compatible with plasmonic waveguides helps with the design of functional devices. Stub resonators, which are finite-length waveguides side-coupled to the input waveguide, are widely used in microwave engineering for impedance matching, filtering, or switching purposes [10]. Due to the similarities between plasmonic waveguides and transmission lines, the stub idea has also been successfully extended to plasmonic applications at optical frequencies. 2D plasmonic single-stub resonators (SSRs) and double-stub resonators (DSRs) have been employed in various applications such as tunable stop band or bandpass filters [11,12], low-power high-contrast switches [13], absorption switches [14], high-performance T-splitters [15], reflectionless step junctions [16], plasmonic demultiplexers [12,17], modulators [18], and observation of plasmonic analog of electromagnetically induced transparency phenomenon [19–23]. Arrays of SSRs or DSRs have also been utilized in developing surface plasmon reflectors [24], or slow-light waveguides [14,19].

Many of the proposed and designed plasmonic devices have used 2D plasmonic MDM waveguides as their platform for three main reasons: a) 2D MDM waveguides have negligible radiation loss at bends or waveguide junctions, which results in their superior performance compared to the 3D waveguides [15,25]; b) MDM waveguides are infinite in one dimension; thus their 2D numerical simulations are easier to handle; c)

a variety of analytical methods such as transmission line theory (TLT) [12,16], scattering matrix theory (SMT) [11,19], and temporal coupled mode theory (CMT) [13] have been successfully applied in the analysis of 2D MDM-based devices. Nonetheless, to fully realize an integrated plasmonic circuit and to avoid cross talk among densely packed components, 2D confinement offered by 3D SWG-based structures is needed. Additionally, SWG-based structures are much more compatible with the integrated circuit fabrication technology than the MDM-based devices. However, a SWG is inherently an open system, such that the introduction of any type of discontinuity along its propagation axis results in scattering and thus radiation loss to the substrate and cladding layers [15]. SWG propagation loss and radiation loss hinder the performance of plasmonic waveguide-integrated structures. The propagation loss can be reduced by decreasing the device footprint to dimensions far less than the propagation length of the waveguide mode; however, suppressing the radiation loss remains an issue to be tackled.

So far, only general properties of 2D MDM waveguides and 3D SWGs, such as dispersion, propagation length, and confinement factors, have been compared [8,15]. However, to the best of our knowledge, systematic comparison between functional 2D and 3D plasmonic devices has not yet been made. Therefore, in this work we compare the performance of 2D and 3D versions of two functional plasmonic devices (i.e., SSRs and DSRs) around the operating wavelength of 1550 nm. In this comparison, 2D structures utilize MDM waveguides; 3D structures utilize SWGs.

It should be noted that some remedies have been posed to avoid radiation losses at the 3D terminated ends (TEs). For instance, in [26], stub resonators based on 3D plasmonic coaxial waveguides with performance close to their MDM counterparts have been offered. In another attempt, a SWG with a high aspect ratio cross-section has been used as the device platform [27,28]. However, fabrication of plasmonic coaxial waveguides or high-aspect-ratio structures in a manner compatible with integrated circuit technology is a challenge.

In Section 2, we introduce the 2D and 3D waveguides and SSR and DSR geometries and the nomenclature used to define each structure. In Section 3, we provide an overview of the application of the scattering matrix model to the stub resonators, and we provide the elements of the scattering matrix required for the analysis of each stub resonator. In Section 4, we demonstrate the simulation method for evaluating the reflection and transmission coefficients of the junctions. In Section 5, the numerical and semianalytical results for the comparison of the 2D and 3D structures studied in this work are provided. Finally, we conclude in Section 6.

## 2. STRUCTURES

Schematics of the 2D MDM waveguide and 3D SWG are depicted in Figs. 1(a) and 1(b). In both cases, dielectric parts are silica with a refractive index of 1.44, and metallic parts are gold with a complex dielectric function taken from [29]. Our choice of gold is due to the fact that it is commonly used in experiments. We use a symmetric SWG with identical substrate and superstrate materials (silica), which ensures the existence of

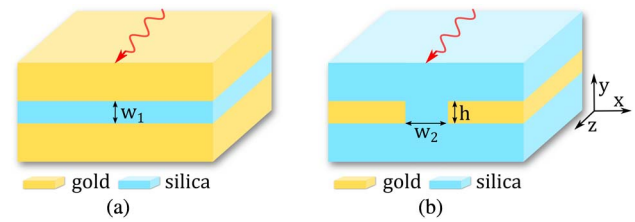


**Fig. 1.** (a) 2D MDM waveguide (gold/silica/gold) with width  $w_1 = 200$  nm; (b) SWG with dimensions  $w_2 \times h = 220$  nm  $\times$  115 nm. The mode propagates in the  $z$ -direction in both cases.

a bound mode for a broadband excitation [8]. The MDM waveguide is infinite in the  $x$ -direction and is confined only in the  $y$ -direction while the SWG is confined in the  $x$ - and  $y$ -directions. The modes propagate along the  $z$ -direction in both geometries.

Bearing in mind the fabrication challenges of narrower gaps, we set the widths of MDM and SWG waveguides to 200 nm and 220 nm, respectively, and then by sweeping over the height of the SWG we found the height  $h = 115$  nm for which the real parts of the effective refractive index of the modes in the two structures were the same at the operating wavelength of 1550 nm. The real part of the complex effective refractive index for the two waveguides is shown in Fig. 2. The intersection point amounts to  $n_{\text{eff}} = 1.6186$  at 1550 nm. The propagation length, defined as  $L_p = 1/\text{imag}(k) = 1/\alpha$ , where  $k = \beta + i\alpha$ , is the complex propagation constant of the waveguide; for our reference MDM waveguide and SWG this amounts to  $22.5 \mu\text{m}$  and  $17.5 \mu\text{m}$  at 1550 nm, respectively. In all the subsequent 2D and 3D simulations, the material properties and the dimensions of the waveguides will be kept fixed. There are other width and height configurations that result in the same  $n_{\text{eff}}$  at 1550 nm; our particular choice is based on having structures that are easy to fabricate. In microwave frequencies, the  $k$  value is critical for stub resonances; that is why we keep  $k$  the same at 1550 nm for MDM and SWG waveguides.

Schematics of the SSRs and DSRs are shown in Fig. 3. In Figs. 3(b) and 3(d), the top silica cladding has been removed for

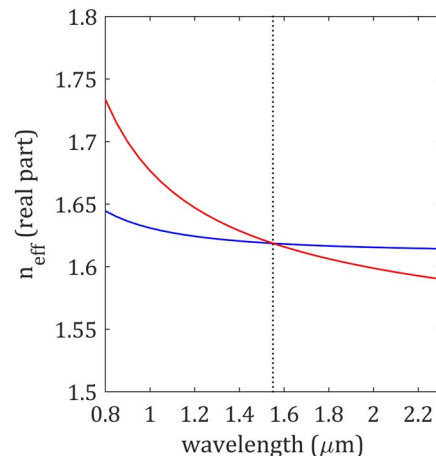


**Fig. 2.** Effective refractive index of MDM waveguide and SWG intersecting at 1550 nm (blue: MDM waveguide, red: SWG)

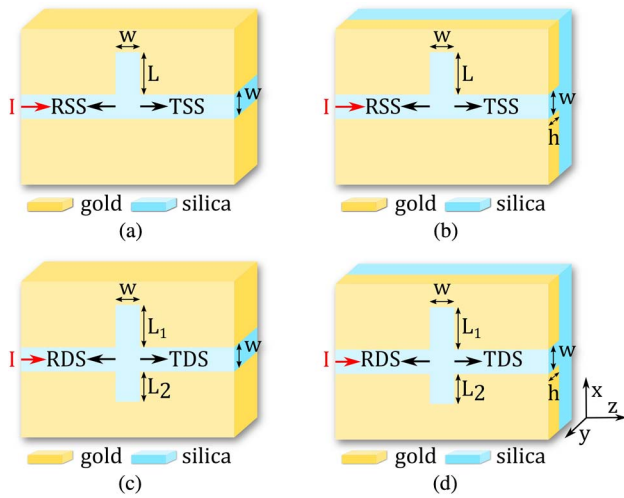


**Fig. 3.** (a) 2D SSR; (b) 3D SSR without top cladding; (c) 2D DSR; (d) 3D DSR without top cladding.

a clearer visualization of the geometry. DSRs are formed by two SSRs located at the same site along the input waveguide, indicating that SSRs are the building blocks of the DSRs.

### 3. ANALYTICAL MODEL

The subwavelength size of our reference waveguides compared to the operating wavelength of 1550 nm ensures their single-mode operation, which is the prerequisite for employing single-mode SMT as a semianalytical model. We applied SMT to analyze the resonator structures.

The SSR is composed of three simple geometries, namely, a T-junction with input from the left, a terminated waveguide, and a T-junction with input from the top, as sketched in Figs. 4(a)–4(c). Complex reflection and transmission coefficients of these geometries are denoted as follows:  $r_1$  is the reflection from the input port of the T-junction (with input from the left),  $t_1$  is the transmission to its straight-output waveguide,

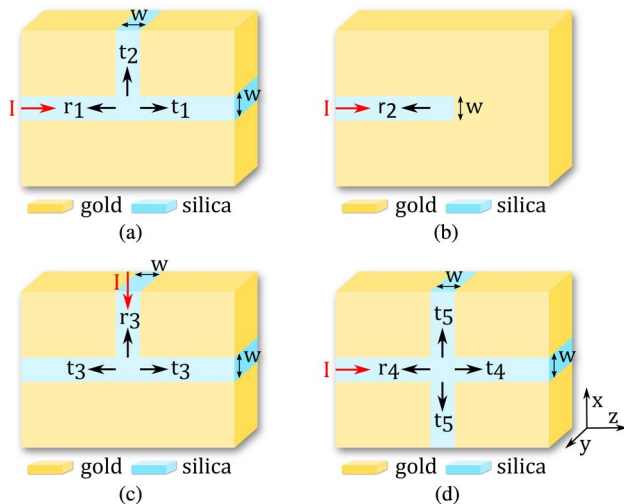


**Fig. 4.** (a) 2D T-junction with input from the left; (b) 2D terminated waveguide; (c) 2D T-junction with input from the top; (d) 2D X-junction.

and  $t_2$  is the transmission to its cross-output waveguide [Fig. 4(a)].  $r_2$  is the reflection from the terminated waveguide [Fig. 4(b)],  $r_3$  is the reflection from the input port of the T-junction (with input from the top), and  $t_3$  gives the corresponding transmission coefficient to its cross-output waveguides [Fig. 4(c)].

With these definitions, the complex transmission (TSS) and reflection (RSS) amplitudes of a SSR with stub length  $L$  are given by [11]

$$\text{TSS} = t_1 + \frac{r_2 t_2 t_3 \exp(2ikL)}{1 - r_2 r_3 \exp(2ikL)}, \quad (1)$$

$$\text{RSS} = r_1 + \frac{r_2 t_2 t_3 \exp(2ikL)}{1 - r_2 r_3 \exp(2ikL)}. \quad (2)$$

The first term in Eq. (1) (i.e.,  $t_1$ ), is the portion of the input SPP wave that directly propagates into the straight-output waveguide of the corresponding T-junction without entering the stub [Fig. 5(a)]. However, the second term gives the contribution from the input SPP wave that enters the stub and then exits to the input waveguide. This term has been derived by the summation of all the transient portions of the incident SPP wave infinitely bouncing back and forth inside the stub to obtain the stationary response [Fig. 5(b)]. The same argument holds for Eq. (2), in which the first term  $r_1$  is the reflection from the left port of the corresponding SPP wave in the stub that is emitted to the left of the input waveguide.

Similarly, SMT has been employed in the derivation of the complex transmission of double-stub resonator (TDS) and reflection of double-stub resonator (RDS) amplitudes of the 2D DSR by deconstructing the DSR as a combination of two geometries: a terminated waveguide and an X-junction as sketched in Figs. 4(b) and 4(d), respectively. For a DSR of stub lengths  $L_1$  and  $L_2$  the TDS and the RDS are given by [14,19]

$$\text{TDS} = t_4 - C, \quad (3)$$

$$\text{RDS} = r_4 - C, \quad (4)$$

where  $C = t_2^2(2t_4 - 2r_4 + s_1 + s_2)/[t_4^2 - (r_4 - s_1)(r_4 - s_2)]$ ,  $s_1 = 1/[r_2 \exp(2ikL_1)]$  and  $s_2 = 1/[r_2 \exp(2ikL_2)]$ . Complex reflection and transmission coefficients of the X-junction are denoted as follows:  $r_4$  is the reflection from the input port of the X-junction,  $t_4$  is the transmission to its

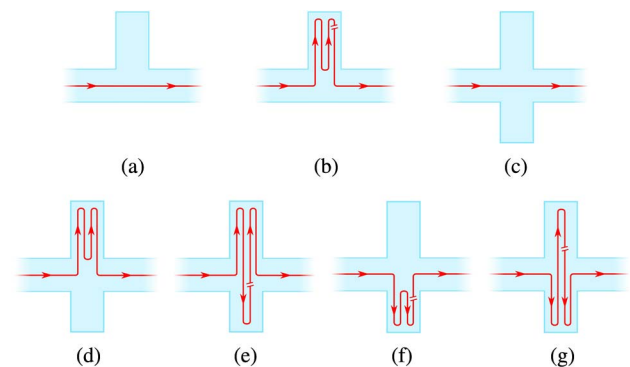


**Fig. 5.** SPP wave scattering pathways in (a,b) SSR; (c–g) DSR.

straight-output waveguide, and  $t_5$  is the transmission to its cross-output waveguide [Fig. 4(d)].

Similar to the SRR, Eqs. (3) and (4) have been derived by assuming the incident SPP wave undergoing five different pathways depicted in Figs. 5(c)–5(g) and described as follows: Fig. 5(c) shows the portion of the incident SPP wave that directly propagates through the X-junction; Fig. 5(d) shows the portion of the incident SPP wave that enters the upper stub, bounces there multiple times and emits out to the right of the input waveguide; Fig. 5(e) shows the portion of the incident SPP wave that enters the upper stub and bounces back and forth in the combined resonator of length  $L_1 + w + L_2$  and then emits out to the right of the input waveguide. Similarly, Fig. 5(f) shows the portion of the input SPP wave that enters the lower stub, bounces there multiple times and emits out to the right of the input waveguide. Finally, Fig. 5(g) shows the portion of the input SPP wave that enters the lower stub and bounces back and forth in the combined resonator of length  $L_1 + w + L_2$  and then emits out to the right of the input waveguide.

#### 4. SIMULATION MODEL

Equations (1)–(4) enable us to predict and investigate the properties of plasmonic SSRs and DSRs without running numerical simulations. This is particularly of importance in 3D structures, which require more simulation time and memory. Furthermore, the equations provide additional insight into the operational principles of SSRs and DSRs.

We used the commercial software package Lumerical FDTD Solutions [30] for numerical simulations of our structures. To utilize Eqs. (1)–(4), first we need to extract all the complex reflection and transmission coefficients of the relevant 2D and 3D geometries [Figs. 4(a)–4(d)]. The methodology for obtaining complex reflection and transmission coefficients of a three-port junction (i.e.,  $r_1$ ,  $t_1$ , and  $t_2$ ) is illustrated in Fig. 6 [31]. The reflection and transmission coefficients of all other geometries are extracted in a similar way.

To allow waveguide modes to form completely and to avoid higher-order modes that might be excited upon reflection or scattering from junctions, in both 2D and 3D simulations

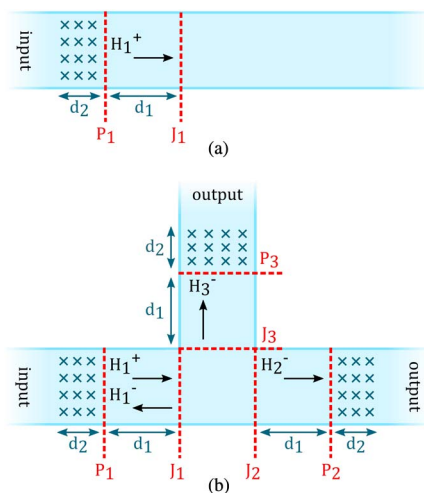


**Fig. 6.** Evaluating (a) incident SPP wave in a straight waveguide; (b)  $r_1$ ,  $t_1$ , and  $t_2$ , complex coefficients in a three-port junction.

SPPs are collected sufficiently away from the waveguide junctions. Therefore, in both 2D and 3D simulations, we set our ports ( $P_1, P_2, P_3$ ),  $d_1 = 1 \mu\text{m}$  away from junctions ( $J_1, J_2, J_3$ ), and by defining a set of point time monitors (PTMs) within  $d_2 = 0.4 \mu\text{m}$  from ports (shown by the cross signs in Fig. 6), we collect time varying magnetic fields from each time monitor and then perform fast Fourier transform (FFT) to obtain the frequency-domain response of each PTM. We calculate the complex transmission and reflection coefficient for each PTM as

$$t = \frac{H_2^-}{H_1^+}, \quad (5)$$

$$r = \frac{H_1^+ + H_1^-}{H_1^+} - 1 = \frac{H_1^-}{H_1^+}. \quad (6)$$

Frequency-domain values of the fields are substituted into these equations and the incident SPP wave;  $H_1^+$ , which is used as normalization, is obtained by running a separate simulation for each of the 2D and 3D straight waveguides [Fig. 6(a)]. We tested our choice of  $d_1 = 1 \mu\text{m}$  by increasing  $d_1$  to  $2 \mu\text{m}$  and observed that the  $r$  and  $t$  coefficients do not change their values.

In 2D simulations, PTMs are distributed in an  $xy$  plane; however, in 3D simulations, they are distributed in an  $xyz$  volume. These monitors are located precisely in input and output ports, such that each time monitor a distance  $d$  away from the input port has an equivalent time monitor a distance  $d$  away from the output port. We evaluate the reflection and transmission coefficients at all these points. We then transform the obtained coefficients to the junction locations ( $J_1, J_2, J_3$ ). We observe that the coefficient values obtained from a collection of points at different locations in the FDTD grid [e.g., to the right of  $P_2$  in Fig. 6(b)] all have very similar values in magnitude and in phase—which ensures that the simulation is set up correctly. We further average the coefficients obtained from different grid locations to get the final values of  $r$  and  $t$  coefficients.

In 2D simulations, we used a uniform mesh of 2 nm in all directions, and in 3D simulations, we used a uniform override mesh of size 5 nm in an  $xyz$  volume surrounding input and stub waveguides and nonuniform mesh elsewhere. The mesh accuracy was set to its default value of two in 3D simulations. Since 2D simulations run quickly, we set the mesh size in 2D simulations to 2 nm. Nonetheless, for our 2D simulations, the mesh size of 5 nm resulted in similar results as those run with 2 nm mesh size. To further check the subtleties of the PTM method, we verified its results with the results obtained with FDTD Solutions' built-in mode expansion monitors (not shown).

## 5. DISCUSSION AND RESULTS

### A. SSRs

By plugging the complex reflection and transmission coefficients of the geometries sketched in Figs. 4(a)–4(c) at 1550 nm into Eq. (1), we plot the 2D and 3D  $|TSS|^2$  versus stub length  $L$ , as shown in Fig. 7. These graphs give us the resonant orders at 1550 nm and assist us in selecting the stub lengths that result in either dips or peaks in the transmission of

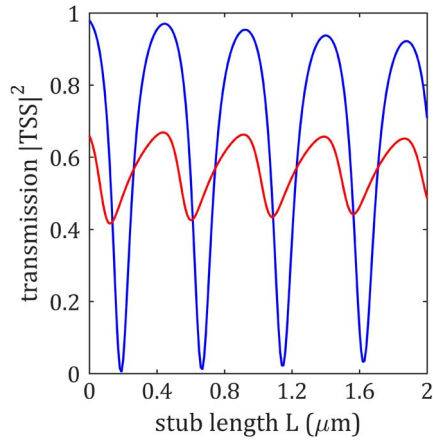


**Fig. 7.** Power transmission  $|TSS|^2$  for 2D (blue curve) and 3D (red curve) SSRs versus stub length.

2D or 3D SSRs at the operating wavelength of 1550 nm. The variations in the single-stub spectrum as a function of  $L$  are due to the interference of the two SPP waves undergoing different pathways: the SPP wave that goes directly through the junction and the ones that bounce within the stub [Figs. 5(a) and 5(b)]. Similarly, by plugging the relevant 2D and 3D complex reflection and transmission coefficients obtained for the wavelength interval  $[0.8, 2.3]$   $\mu\text{m}$  into Eq. (1), we plot the wavelength response for the first four resonant stub lengths corresponding to a dip or a peak in the transmission spectrum at 1550 nm for 2D (Fig. 8) and 3D (Fig. 9) SSRs. The specifications of the resulting SMT-predicted spectra for 2D and 3D SSRs are listed in Table 1 and Table 2. To calculate the Q-factor defined as  $f_0/\text{FWHM}$  and the finesse defined as  $\text{FSR}/\text{FWHM}$ , where  $f_0$  is the resonant frequency, FWHM is the full width at half-maximum of the spectrum and FSR is the free spectral range, we plotted spectra in frequency domain to evaluate the FWHM and FSR parameters. The Q-factors of the spectra with dips have been calculated by inverting the spectra via the operation  $\max(\text{spectrum}) - \text{spectrum}$ . From the information provided in these tables, we see that the spectra which feature dips have less FWHM compared to the spectra that feature peaks.

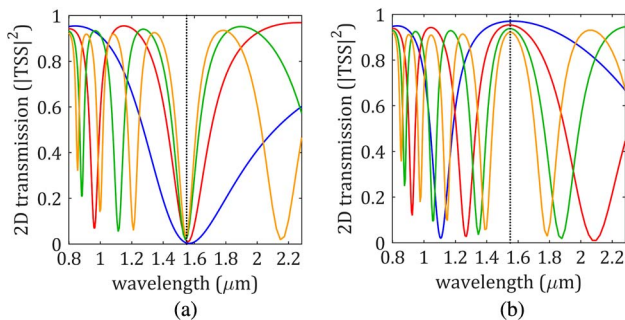


**Fig. 8.** (a) First four resonant orders corresponding to a dip in 2D SSR spectrum at 1550 nm (blue:  $L = 190$  nm, red: 670 nm, green: 1140 nm, yellow: 1620 nm); (b) first four resonant orders corresponding to a peak in 2D SSR spectrum at 1550 nm (blue:  $L = 450$  nm, red: 920 nm, green: 1400 nm, yellow: 1880 nm).

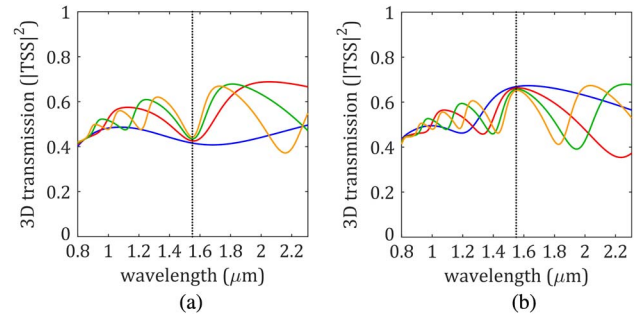


**Fig. 9.** (a) First four resonant orders corresponding to a dip in 3D SSR spectrum (blue:  $L = 120$  nm, red: 600 nm, green: 1080 nm, yellow: 1560 nm); (b) first four resonant orders corresponding to a peak in 3D SSR spectrum (blue:  $L = 440$  nm, red: 910 nm, green: 1390 nm, yellow: 1870 nm).

We found that in both the 2D and 3D spectra with either dips or peaks, longer stub lengths resulted in narrower FWHM but slightly lower contrast. This means that there is a trade-off between the device footprint and its optimum performance. This observation originates from the fact that a SSR can be assumed as a Fabry–Perot (FP) resonator with partially reflecting mirrors of fixed reflection coefficients  $r_1$  and  $r_2$  for a specific wavelength. In a Fabry–Perot resonator, the resonator FWHM linewidth is given by  $\Delta\nu = c\alpha_r/2\pi$ , where  $\alpha_r$  is the effective

**Table 1.** 2D SSRs<sup>a</sup>

$L_{\text{dip}}$ (nm)	FWHM (nm)	Q-Factor	Finesse
190	800	2.13	-
670	270	5.80	3.60
1140	170	9.29	3.57
1620	120	12.52	3.53
$L_{\text{peak}}$ (nm)	FWHM (nm)	Q-Factor	Finesse
450	1101	1.56	1.40
920	577	2.84	1.36
1400	376	4.23	1.38
1880	279	5.66	1.36

<sup>a</sup>Spectrum specifications of first four resonant orders resulting in a dip or a peak at 1550 nm in 2D SSR power transmission.

**Table 2.** 3D SSRs<sup>a</sup>

$L_{\text{dip}}$ (nm)	FWHM (nm)	Q-Factor	Finesse
120	-	-	-
600	467	2.99	-
1080	260	5.69	2.25
1560	182	8.24	2.32
$L_{\text{peak}}$ (nm)	FWHM (nm)	Q-Factor	Finesse
440	-	-	-
910	907	2.10	0.95
1390	550	3.18	1
1870	400	4.22	1

<sup>a</sup>Spectrum specifications of first four resonant orders resulting in a dip or a peak at 1550 nm in 3D SSR power transmission.

total distributed-loss coefficient given by  $\alpha_r = 1/L_p + (1/2L)\ln(1/r_1r_2)$  [32,33]. As a result, by increasing  $L$ , the FWHM decreases.

It is also evident (Fig. 7) that the transmission contrast (i.e., the difference between minimum and maximum power levels which is a requisite for having high performance switches and filters) is far less in the 3D SSR than the 2D SSR. This quantity varies between 0.43 and 0.67 for the 3D SSR, while for a 2D SSR, the corresponding value varies between nearly 0 and 0.92. Furthermore, the 2D and 3D SSRs, which are designed to be equivalent at 1550 nm, show peaks in their spectra for almost the same stub lengths, but the dip in their spectra occurs for different stub lengths. The peak values corresponding to different stub lengths amount almost to the transmitted powers of the straight waveguides ( $L = 0$ ) in both 2D and 3D cases. However, the dip values in the 2D case almost reach zero, and in the 3D case, it reaches 0.43.

The low contrast and the shift in dip resonances in the 3D case can be explained by understanding the operational principle of the SSR. To understand the operational mechanism of SSRs, in Fig. 10(a) we show the transmitted power of a 2D SSR versus stub length  $L$  at 1550 nm (blue line) along with two different phase plots, all obtained by SMT: a) phase difference between the SPP wave passing directly through the junction and the SPP wave coming back from the stub (yellow line), which in fact is the phase difference between the first and second terms of the Eq. (1); b) round-trip phase shift (red line) that the SPP wave entering the stub gains in the stub given by  $\varphi_{r_2}(\lambda) + 2k(\lambda)L + \varphi_{r_3}(\lambda)$ , where  $\varphi_{r_2}(\lambda)$  is the phase shift that the SPP wave experiences upon reflection from the TE of the stub,  $\varphi_{r_3}(\lambda)$  is the phase shift experienced by the SPP wave as it reflects from the T-junction with input from the top, and  $2k(\lambda)L$  is the round-trip phase shift that the SPP wave gains as it propagates along a stub of length  $L$ .

The phase analysis of the two SPP waves propagating along two different pathways in a SSR [Figs. 10(a) and 10(b)] reveals that when the phase difference between the two SPP waves (yellow line) is  $2\pi(\pi)$ , there is a peak (dip) in the transmitted power. Moreover, when there is a dip in the transmission, the round-trip phase gained by the SPP wave inside the stub is  $2\pi$ . Therefore, in the formation of a dip, the SPP wave that enters the stub undergoes constructive interference and bounces multiple times inside the stub before coming out. In this case, due to the open nature of the 3D SSR, the SPP wave

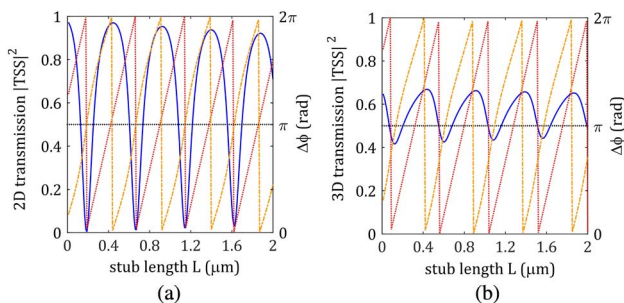


**Fig. 10.** Relation between the variation of the transmission amplitude (blue line) and the evolution of phases (red and yellow lines) versus stub length  $L$  in (a) 2D SSR; (b) 3D SSR.

suffers more from the radiation loss compared to the case when it does not undergo constructive interference inside the stub. Consequently, the attenuated SPP wave leaving the stub has smaller amplitude compared to the SPP wave that directly passes through the junction, which results in a poor destructive interference between the two waves despite being out of phase and thus low contrast. A similar argument holds for the case when we have a peak in the transmission. The peak transmission in the 3D case is lower compared to the 2D case because the SPP wave that enters the stub loses almost half of its power in the first round, which causes poor constructive interference between the two SPP waves that undergo different pathways despite being in phase.

The main reason behind the shift in the resonant lengths corresponding to dips in 3D case with respect to the 2D case is due to the fact that, when there is a dip, the SPP wave circulating in the stub satisfies the resonance condition given by  $\varphi_{r_2}(\lambda) + 2k(\lambda)L + \varphi_{r_3}(\lambda) = 2m\pi$  ( $m = 0, 1, 2, \dots$ ) [red line in Fig. 10(a)]. Comparison of the phases of  $r_2$  and  $r_3$  coefficients in 2D and 3D cases (not shown) reveals that in 3D,  $\varphi_{r_2}(\lambda) + \varphi_{r_3}(\lambda)$  contribution is larger compared to 2D; hence, a shorter  $L$  value suffices to reach the resonance.

Another point is that the resonant dips and peaks that occur at wavelengths other than 1550 nm in the SMT-predicted spectra (Figs. 8 and 9) do not overlap as the resonance order increases. By changing the stub length, the FSR, and accordingly, the location of the resonances changes. In ideal FP resonators that are all resonant at a given wavelength  $\lambda_0$ , the resonators with higher resonance orders are expected to fit an integer amount of peaks/dips in between the peaks/dips of the resonator with the lowest order. However, in our case, the resonance condition has the general form  $\varphi_{r_2}(\lambda) + 2k(\lambda)L + \varphi_{r_3}(\lambda) = m\pi$  ( $m = 0, 1, 2, \dots$ ) with dispersive  $k$  and  $\varphi_{r_2}(\lambda)$  and  $\varphi_{r_3}(\lambda)$  values, which leads to deviations from the ideal FP model.

We verified the prediction of SMT with numerical FDTD simulations. We simulated 2D and 3D SSRs with stub lengths both set to the third resonant length of the 3D SSR at 1550 nm (i.e.,  $L = 1.39 \mu\text{m}$ ), as predicted by SMT in Table 2. The simulation results shown in Figs. 11(a) and 11(b) verify the predictions of SMT and its applicability to the 3D structures.

The obtained semianalytic and numeric results reveal the low capability of 3D SSRs for being used in switching and filtering purposes compared to 2D SSRs. This is mostly due to

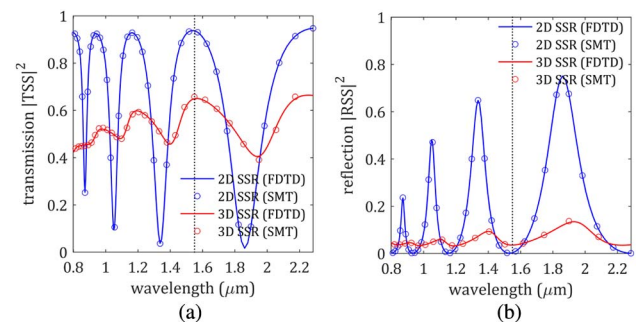


**Fig. 11.** (a) Transmission; (b) reflection coefficients of 2D and 3D SSRs with stub length  $L = 1390 \text{ nm}$  predicted by SMT and verified with numerical FDTD simulations.

the low contrast of the 3D SSR transmission spectrum. A couple of solutions have been offered to either reduce the radiation losses at the 3D TEs and thus increase the contrast of a 3D SSR or design a slit-like 3D plasmonic filter. For instance, in [34], the stub region has been filled with a high-refractive index material. This increases the confinement of the mode in the stub region and the contrast of the transmission spectrum. Another way of increasing the contrast of the 3D SSR is to increase the height of the SWG metallic layer to 1–3  $\mu\text{m}$  while keeping its width as small as 50 nm [27,28]. The narrower gap for 3D SWGs provides more confinement and improves device performance. To get around the radiation losses, a 3D slit-like plasmonic filter in thin metallic layers has been designed and has been shown to be more successful than the 3D SSR [28,35].

## B. DSRs

Similar to the SSR, by substituting the complex reflection and transmission coefficients at 1550 nm of the relevant geometries [Figs. 4(b) and 4(d)] into Eq. (3), we plot the power transmission coefficient,  $|\text{TDS}|^2$ , for the 2D and 3D DSRs versus stub lengths  $L_1$  and  $L_2$  both ranging from 0 to 2  $\mu\text{m}$ , as shown in Figs. 12(a) and 12(b), respectively.

These transmission maps depict the resonant orders for which there is either a dip or a peak in the power transmission of DSRs, and thus are helpful in choosing the appropriate stub lengths, depending on the application.

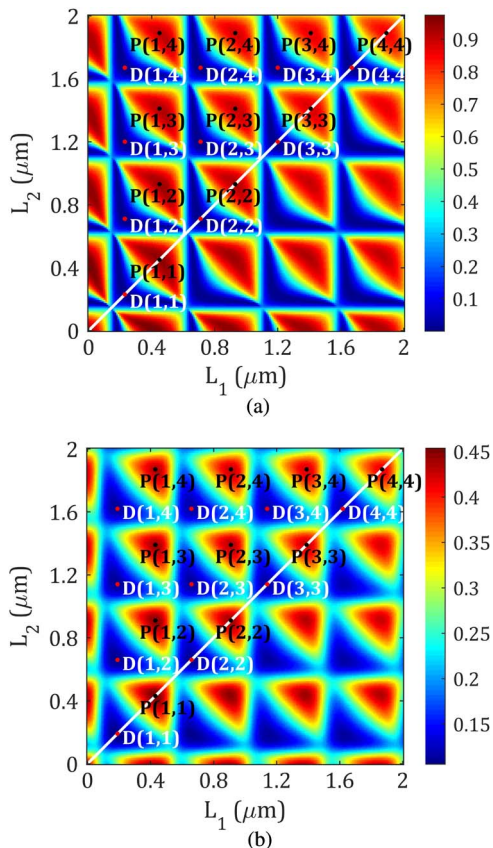


**Fig. 12.** Power transmission  $|\text{TDS}|^2$  versus  $L_1$  and  $L_2$  at 1550 nm for the (a) 2D DSR; (b) 3D DSR.

Due to the symmetry of the geometry, we focus only on the length pairs that lie above the  $L_1 = L_2$  line, shown by the white line. The resonant orders corresponding to peaks (dips) in transmission are denoted by black (red) dots and the letters P (D).

In the DSRs, the incident SPP wave has the opportunity to propagate through five different pathways, as illustrated in Figs. 5(c)–5(g). Variation of the power transmission versus stub lengths originates from the fact that, for some length pairs, the five SPP waves interfere constructively (destructively) to form a peak (dip) in the resulting power transmission spectrum.

Moreover, in the  $|\text{TDS}|^2$  plots,  $L_1 = 0$  and  $L_2 = 0$  axes, which due to symmetry are identical, give the power transmission spectrum of the SSR at 1550 nm with stub length ranging from 0 to 2  $\mu\text{m}$ . It is clear that along these axes, the length interval for which we have a dip in the transmission spectrum of the SSR is less than the length interval for which we have a peak. As tuning of stub length is analogous to the tuning of wavelength, this further proves that spectral FWHM of the SSR, which features a dip in transmission, is narrower than the one that features a peak in the transmission.

In Figs. 13(a) and 13(b), we plot the SMT-predicted spectra of the 2D DSR  $|\text{TDS}|^2$  for the first four resonant orders of equal stub lengths that result in a peak [denoted as  $P(1, 1)$ ,  $P(2, 2)$ ,  $P(3, 3)$ ,  $P(4, 4)$  in Fig. 12(a)], or a dip [denoted as  $D(1, 1)$ ,  $D(2, 2)$ ,  $D(3, 3)$ ,  $D(4, 4)$  in Fig. 12(a)], respectively. Similarly, in Figs. 14(a) and 14(b), we show the predicted spectra of the equivalent resonant orders for the 3D DSR. Similar to 3D SSRs, the peak amplitude of the 3D DSR is almost half of the 2D DSR, and its contrast is lower compared to the 2D DSR.

Table 3 and Table 4 list the equal resonant length pairs that result in either a dip or a peak in the 2D and 3D DSRs, along with the specifications of their corresponding spectra obtained by scattering matrix formalism. The comparison reveals that similar to the SSRs, the resonant orders corresponding to peaks (at 1550 nm) happen almost at the same stub lengths, regardless of being 2D or 3D structures; however, the resonant orders corresponding to dips (at 1550 nm) happen at slightly different length pairs. Comparison of the results provided in Table 2 for the 3D SSR and Table 4 for the 3D DSR reveals that SSRs and

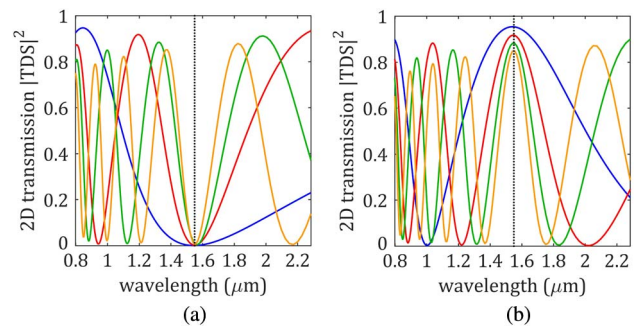


**Fig. 13.** (a) Blue line:  $L_1 = L_2 = 0.23 \mu\text{m}$ , red line:  $L_1 = L_2 = 0.71 \mu\text{m}$ , green line:  $L_1 = L_2 = 1.2 \mu\text{m}$ , yellow line:  $L_1 = L_2 = 1.67 \mu\text{m}$ ; (b) blue line:  $L_1 = L_2 = 0.45 \mu\text{m}$ , red line:  $L_1 = L_2 = 0.93 \mu\text{m}$ , green line:  $L_1 = L_2 = 1.41 \mu\text{m}$ , yellow line:  $L_1 = L_2 = 1.89 \mu\text{m}$ . Black dotted line specifies the location of the operating wavelength, 1550 nm.

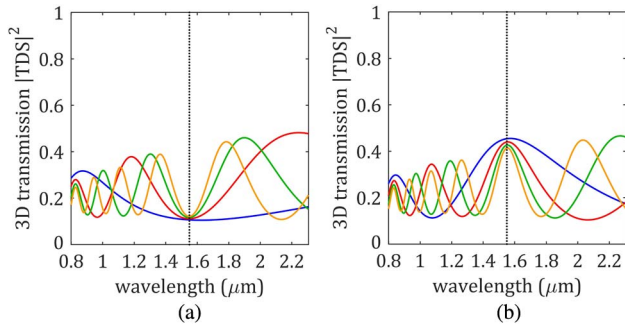


**Fig. 14.** (a) Blue line:  $L_1 = L_2 = 0.19 \mu\text{m}$ , red line:  $L_1 = L_2 = 0.66 \mu\text{m}$ , green line:  $L_1 = L_2 = 1.14 \mu\text{m}$ , yellow line:  $L_1 = L_2 = 1.62 \mu\text{m}$ ; (b) blue line:  $L_1 = L_2 = 0.43 \mu\text{m}$ , red line:  $L_1 = L_2 = 0.91 \mu\text{m}$ , green line:  $L_1 = L_2 = 1.39 \mu\text{m}$ , yellow line:  $L_1 = L_2 = 1.879 \mu\text{m}$ . Black dotted line specifies the location of the operating wavelength, 1550 nm.

DSRs show a peak in their transmission at the same stub lengths; however, DSRs featuring a peak (dip) in their spectra have narrower (wider) FWHM, and thus higher (lower)  $Q$ -factor compared to their corresponding SSRs. The comparison of Figs. 9(b) and 14(b) also shows that DSRs provide us with better contrast compared to SSRs.

Starting from second resonant order of equal length pairs  $P(2, 2)$  denoted as point A, in Figs. 15(a) and 15(b), and moving away from this peak point along the symmetry axis, which

ensures the equality of the stub lengths, in Figs. 15(c) and 15(d) we show how to tune the resonant wavelength in both 2D and 3D DSRs, respectively. As expected, by increasing the stub lengths, the resonant wavelength undergoes a red shift.

Our analysis shows that in both types of resonant orders (dips or peaks) in both 2D and 3D DSRs, by increasing the stub length, the FWHM of the resulting spectrum decreases. This again originates from the Fabry–Perot effect already explained in Section 5.A. It is worth noting that the same behavior occurs for a DSR of unequal stub lengths, such that by keeping one stub length fixed and increasing the length of the second stub, the FWHM decreases (not shown). For instance,  $P(1, 3)$  has narrower FWHM compared to the  $P(1, 2)$ . However, in a DSR of unequal stub lengths, some extra lobes and shoulders appear in the spectrum, unlike in a DSR of equal lengths. Therefore, we inspected only DSRs of equal stub lengths, which produce neat and uniform spectra.

Further, we found that, while tuning within each resonant order, the spectrum FWHM remains almost unchanged; however, the change in FWHM is far more from one resonant order to another.

Utilizing the transmission maps of Figs. 12(a) and 12(b), we can further locate the points that result in the plasmonic induced transparency (PIT) phenomenon [19]. To observe this phenomenon, we should start from an equal stub length pair with the DSR and the corresponding SSRs simultaneously having a dip in the transmitted power [36]. These points are depicted with white dots in Figs. 16(a) and 16(b) for 2D and 3D

**Table 3. 2D DSRs<sup>a</sup>**

$L_1 = L_2 = L_{\text{dip}}$ (nm)	FWHM (nm)	Q-Factor	Finesse
230	1182	1.38	-
710	515	3.16	2.04
1200	308	5.18	2.03
1670	217	7.23	2.07
$L_1 = L_2 = L_{\text{peak}}$ (nm)	FWHM (nm)	Q-Factor	Finesse
450	821	1.92	-
930	397	3.9	1.90
1410	264	5.85	1.90
1890	199	7.73	1.87

<sup>a</sup>Spectrum specifications of first four resonant orders resulting in a dip or a peak at 1550 nm in 2D DSR power transmission.

**Table 4. 3D DSRs<sup>a</sup>**

$L_1 = L_2 = L_{\text{dip}}$ (nm)	FWHM (nm)	Q-Factor	Finesse
190	-	-	-
660	586	2.65	1.60
1140	339	4.56	1.68
1620	238	6.50	1.77
$L_1 = L_2 = L_{\text{peak}}$ (nm)	FWHM (nm)	Q-Factor	Finesse
430	880	1.94	1.67
910	426	3.75	1.70
1390	288	5.46	1.72
1870	221	7.07	1.64

<sup>a</sup>Spectrum specifications of first four resonant orders resulting in a dip or a peak at 1550 nm in 3D DSR power transmission.

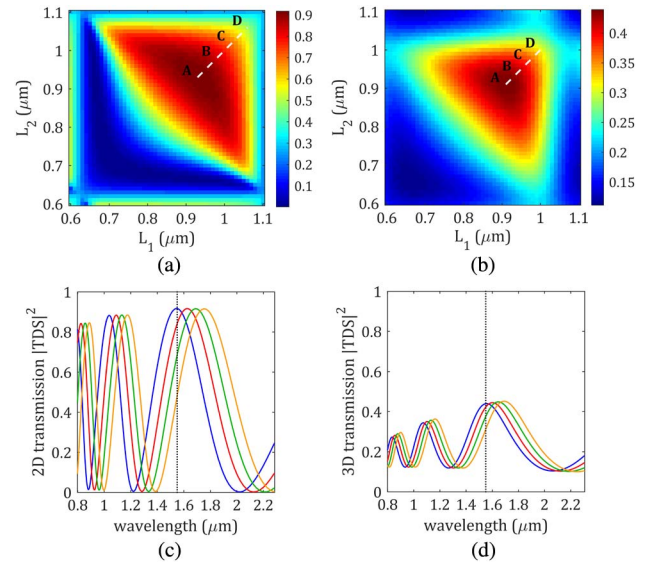


**Fig. 15.** Four sets of equal-length pairs chosen from second resonant order along the symmetry axis of the transmission map of (a) 2D DSR; (b) 3D DSR. Power transmission spectra of (c) 2D DSR for length pairs A:  $L_1 = L_2 = 930 \text{ nm}$  (blue line,  $\lambda_{\text{peak}} = 1550 \text{ nm}$ ), B:  $L_1 = L_2 = 980 \text{ nm}$  (red line,  $\lambda_{\text{peak}} = 1626 \text{ nm}$ ), C:  $L_1 = L_2 = 1020 \text{ nm}$  (green line,  $\lambda_{\text{peak}} = 1690 \text{ nm}$ ), D:  $L_1 = L_2 = 1060 \text{ nm}$  (yellow line,  $\lambda_{\text{peak}} = 1752 \text{ nm}$ ); (d) 3D DSR for length pairs A:  $L_1 = L_2 = 910 \text{ nm}$  (blue line,  $\lambda_{\text{peak}} = 1550 \text{ nm}$ ), B:  $L_1 = L_2 = 940 \text{ nm}$  (red line,  $\lambda_{\text{peak}} = 1600 \text{ nm}$ ), C:  $L_1 = L_2 = 970 \text{ nm}$  (green line,  $\lambda_{\text{peak}} = 1650 \text{ nm}$ ), D:  $L_1 = L_2 = 1000 \text{ nm}$  (yellow line,  $\lambda_{\text{peak}} = 1690 \text{ nm}$ ).

DSRs, respectively. The PIT effect is observed by breaking the symmetry of the DSR, which is possible by making stub lengths slightly unequal while keeping the total length constant. Asymmetric DSRs of slightly unequal stub lengths allow the formation of an asymmetric mode in the combined resonator of length  $L_1 + w + L_2$  ( $w$  being the width of the waveguide) in addition to the symmetric mode and paves the way for their coupling, which is the origin of the Fano-shaped transparency window in the PIT phenomenon [18].

Taking into account the fact that the resonant wavelength in the PIT phenomenon, for which a peak in the transmission appears, is proportional to the combined resonator length, by increasing one stub length by an amount of  $dL$  and decreasing the other stub length by the same amount, we can keep the total resonator length and thus PIT resonant wavelength fixed. This is possible by moving along the dashed white lines [Figs. 16(a) and 16(b)], which pass through PIT(1, 1) and PIT(2, 2) resonant orders and make an angle of  $45^\circ$  with horizontal and vertical axes.

Starting from PIT(1, 1) and moving along the dashed white line [Fig. 16(a)] with steps of  $dL = 10$  nm, in Fig. 16(c) we show the spectra of the 2D DSR for four sets of unequal length pairs. The dashed black curve gives the power transmission of the 2D DSR of equal stub lengths, which, due to the finite and rather wide width of our reference plasmonic MDM waveguide is not zero at 1550 nm [18,36]. We found that by increasing  $dL$ , the asymmetry factor remains the same but the transmission amplitude increases [18,36].

Starting from PIT(1, 1) for 3D DSRs and moving along the dashed white line [Fig. 16(b)], we tried the same approach in the 3D DSR; however, we could not observe any reasonable asymmetric Fano-shaped transparency window for this PIT

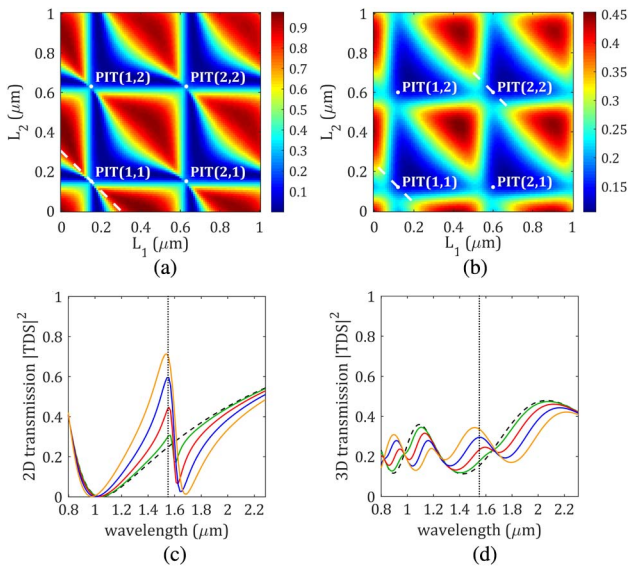


**Fig. 16.** PIT locations for (a) 2D DSR; (b) 3D DSR. Asymmetric PIT-type spectra. (c) 2D DSR (black dashed curve:  $L_1 = L_2 = (150, 150)$  nm, green:  $(160, 140)$  nm, red:  $(170, 130)$  nm, blue:  $(180, 120)$  nm, yellow:  $(190, 110)$  nm); (d) 3D DSR (black dashed curve:  $L_1 = L_2 = (600, 600)$  nm, green:  $(630, 570)$  nm, red:  $(660, 540)$  nm, blue:  $(690, 510)$  nm, yellow:  $(720, 480)$  nm).

resonant order. We tried PIT(2, 2), and the resulting spectra for four different sets of unequal stub lengths with steps of  $dL = 30$  nm are shown in Fig. 16(d). We conclude that observing PIT in 3D DSRs is almost impossible, which might be due to the open nature of 3D SWGs that does not allow the formation of well-defined junction resonator modes [18].

Although we could not observe the PIT phenomenon in the studied 3D DSR, the PIT phenomenon has been observed in slightly decoupled stub pairs attached to a U-shaped 3D plasmonic waveguide [37].

A comparison of the reflection and transmission coefficients of the 2D geometries of Figs. 4(a)–4(d) with their 3D counterparts (results not shown) reveal that the  $r_2$  coefficient—which is the reflection from a terminated waveguide end—is far less in the 3D terminated end than in the 2D one, compared to all the other reflection and transmission coefficients. This is a sign of significant radiation loss in the 3D TEs. One way for increasing the  $r_2$  coefficient is to increase the height of the metallic layer, which converts the 3D SWG to an MDM waveguide, or adding block reflectors as high as  $1 \mu\text{m}$  to the TEs [38,39]. Nonetheless, the latter approach not only adds complexity to the fabrication of the TEs but also increases the device footprint.

At the TEs, the 3D SWG is abruptly converted to a dielectric-metal-dielectric (DMD) waveguide. Due to the mismatch between the modal shapes of the SWG and DMD waveguide, the SPP wave partially scatters to the cladding and substrate layers and partially is coupled to the MD and DMD modes. Therefore, one way to boost the  $r_2$  reflection coefficient is to add a curved grating to the TE to reflect back the portion of the mode that is coupled to the DMD waveguide modes. We adapted the curved grating design in Ref. [40], and we saw some improvement in the  $r_2$  coefficient and a 10% increase in the transmitted power of the DSR (results not shown). Regardless of how well the curved grating in a DMD waveguide is designed, due to the finite height of the grating blades, the reflected SPP wave will suffer from radiation loss as it propagates through them. Moreover, the addition of a grating increases the device footprint, which is a detriment.

Another method that we tried for boosting the  $r_2$  reflection coefficient was to add a DSR to the TE, as shown in Fig. 17(a). According to the transmission map of the 3D DSR [Fig. 12(b)], the length pairs that result in a dip in the transmission of the DSR result in a peak in the reflection spectrum. Hence, by adding a DSR with a dip in its transmission and thus a peak in its reflection to the TE, we can expect an increase in the  $r_2$  reflection coefficient.

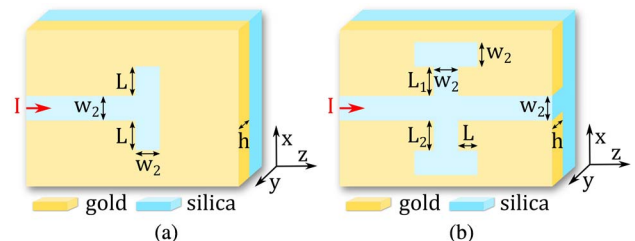


**Fig. 17.** (a) TE with a DSR; (b) DSR with DSR at the end of its stubs.

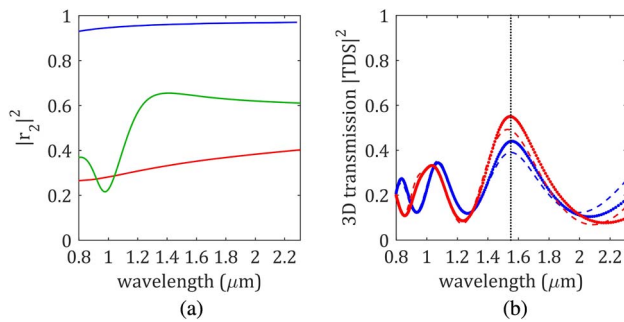


**Fig. 18.** (a) Comparison of the reflection coefficients of TEs. Blue line: 2D TE, red line: 3D TE, green line: 3D TE with double stub at its end; (b) comparison of the  $|TDS|^2$  results. Blue curve: P(2,2) resonator as in Fig. 3(d), red curve: P(2,2) resonator with double-stub-terminated stubs as in Fig. 17(b). Solid lines are scattering matrix results and dashed lines are calculated numerically with 3D FDTD simulations.

In Fig. 18(a), we compare the  $r_2$  reflection coefficient, evaluated with numerical FDTD simulations, for 2D and 3D TEs along with the  $r_2$  reflection coefficient of a terminated end with a DSR [Fig. 17(a)] with stub lengths  $L = 190$  nm corresponding to the first order dip  $D(1, 1)$ , shown in Fig. 12(b). As can be seen, the  $r_2$  reflection coefficient for the 2D terminated end is much higher than the 3D TE, and the 2D TE acts almost like a perfect mirror. Furthermore, it is evident that adding a DSR to the 3D TE increases the  $r_2$  reflection coefficient. While  $r_2$  is designed to be maximum at 1550 nm, due to the finite width of the reflection maximum of a DSR with  $L = 190$  nm stubs, there is a dip at 980 nm in the  $r_2$  coefficient of the double stub terminated end [green curve in Fig. 18(a)].

A schematic of a DSR with a double stub at the end of its stubs is shown in Fig. 17(b). Any change in the  $r_2$  reflection coefficient affects the transmission map of the DSR such that the locations of the resonant length pairs that correspond to dips or peaks change. By reevaluating the transmission map for a DSR (with double-stub terminations at the end of its stubs), we selected the length pairs  $L_1 = L_2 = 680$  nm corresponding to the second-order peak  $P(2, 2)$  in its power transmission map (not shown) to be able to compare its transmitted power spectrum with the transmitted power spectrum of a DSR (without double-stub terminations at the end of its stubs) with stub lengths  $L_1 = L_2 = 910$  nm corresponding to a second-order peak in its power transmission map. The comparison of the two cases [Fig. 18(b)] reveals that the addition of a DSR to the stub ends improves the spectrum contrast as well as the transmission amplitude.

## 6. CONCLUSIONS

In this work, we compared resonators made of 3D SWGs with their 2D MDM waveguide counterparts. To that end, we analyzed plasmonic SSR and DSR geometries.

We have shown that SMT can be applied to open 3D SWG-based devices, and we verified the predicted features with numerical FDTD simulations. This finding provides us with a powerful tool for predicting and manipulating the spectra of the 3D resonators by selecting the right stub lengths without

the need to sweep over stub dimensions via full 3D FDTD simulations.

We found that, despite the existence of radiation loss, which degrades the performance of 3D structures, by a careful selection of resonator dimensions, 3D structures can have characteristics similar to those of 2D structures. We investigated designs for reducing radiation loss in 3D SWGs. We provided a double stub-based waveguide termination design that enhanced the resonator properties.

The relatively thin metallic layer (115 nm) and the uniform silica ambient ( $n = 1.44$ ) of the 3D resonators lead to rather low  $Q$  values. However, filling the stubs with a high-index material can boost the quality factor and improve the contrast of the 3D resonators by reducing the radiation loss [34]. Furthermore, increasing the thickness of the metal to 1000 nm or more reduces the radiation loss significantly [27]. Stub resonators with low  $Q$  but with high concentration of fields can be of use in detector designs in optical interconnect applications that require very low energy consumption [41].

Plasmonic sensors usually have low  $Q$  values; however, they are very sensitive to the refractive index profile surrounding them and operate by detecting the change in the resonance frequency due to the perturbation of the local refractive index [42]. A biosensor based on a 3D plasmonic SWG has already been proposed [43]; the addition of stub resonators integrated in SWGs can further boost the sensor's figure of merit by providing extra knobs to shape the spectral properties. The 3D DSRs can further be utilized in the investigation of light-matter interactions in quantum plasmonic applications via positioning colloidal quantum dot emitters in hotspots within the DSR [39].

**Funding.** Scientific and Technological Research Council of Turkey (TUBITAK) (112E247).

## REFERENCES

1. L. Novotny and B. Hecht, *Principles of Nano-Optics* (Cambridge University, 2012).
2. J. A. Dionne, L. A. Sweatlock, H. A. Atwater, and A. Polman, "Plasmon slot waveguides: towards chip-scale propagation with subwavelength-scale localization," *Phys. Rev. B* **73**, 035407 (2006).
3. J.-C. Weeber, A. Dereux, C. Girard, J. R. Krenn, and J.-P. Goudonnet, "Plasmon polaritons of metallic nanowires for controlling submicron propagation of light," *Phys. Rev. B* **60**, 9061–9068 (1999).
4. M. L. Brongersma, J. W. Hartman, and H. A. Atwater, "Electromagnetic energy transfer and switching in nanoparticle chain arrays below the diffraction limit," *Phys. Rev. B* **62**, R16356 (2000).
5. V. R. Almeida, Q. Xu, C. A. Barrios, and M. Lipson, "Guiding and confining light in void nanostructure," *Opt. Lett.* **29**, 1209–1211 (2004).
6. D. K. Gramotnev and D. F. P. Pile, "Single-mode subwavelength waveguide with channel plasmon-polaritons in triangular grooves on a metal surface," *Appl. Phys. Lett.* **85**, 6323–6325 (2004).
7. G. Veronis and S. Fan, "Guided subwavelength plasmonic mode supported by a slot in a thin metal film," *Opt. Lett.* **30**, 3359–3361 (2005).
8. G. Veronis and S. Fan, "Modes of subwavelength plasmonic slot waveguides," *J. Lightwave Technol.* **25**, 2511–2521 (2007).
9. A. Boltasseva, V. S. Volkov, R. B. Nielsen, E. Moreno, S. G. Rodrigo, and S. I. Bozhevolnyi, "Triangular metal wedges for subwavelength plasmon-polariton guiding at telecom wavelengths," *Opt. Express* **16**, 5252–5260 (2008).
10. M. D. Pozar, *Microwave Engineering* (Wiley, 2012).

11. X.-S. Lin and X.-G. Huang, "Tooth-shaped plasmonic waveguide filters with nanometric sizes," *Opt. Lett.* **33**, 2874–2876 (2008).
12. Y. Matsuzaki, T. Okamoto, M. Haraguchi, M. Fukui, and M. Nakagaki, "Characteristics of gap plasmon waveguide with stub structures," *Opt. Express* **16**, 16314–16325 (2008).
13. X. Piao, S. Yu, S. Koo, K. Lee, and N. Park, "Fano-type spectral asymmetry and its control for plasmonic metal-insulator-metal stub structures," *Opt. Express* **19**, 10907–10912 (2011).
14. Y. Huang, C. Min, L. Yang, and G. Veronis, "Nanoscale plasmonic devices based on metal-dielectric-metal stub resonators," *Int. J. Opt.* **2012**, 1–13 (2012).
15. W. Cai, W. Shin, S. Fan, and M. L. Brongersma, "Elements for plasmonic nanocircuits with three-dimensional slot waveguides," *Adv. Mater.* **22**, 5120–5124 (2010).
16. A. Pannipitiya, I. D. Rukhlenko, and M. Premaratne, "Analytical modeling of resonant cavities for plasmonic-slot-waveguide junctions," *IEEE Photon. J.* **3**, 220–233 (2011).
17. Z. Chen, R. Hu, L. Cui, L. Yu, L. Wang, and J. Xiao, "Plasmonic wavelength demultiplexers based on tunable Fano resonance in coupled-resonator systems," *Opt. Commun.* **320**, 6–11 (2014).
18. X. Piao, S. Yu, and N. Park, "Control of Fano asymmetry in plasmon induced transparency and its application to plasmonic waveguide modulator," *Opt. Express* **20**, 18994–18999 (2012).
19. Y. Huang, C. Min, and G. Veronis, "Plasmon-induced transparency in subwavelength metal-dielectric-metal waveguides," *Proc. SPIE* **7941**, 79410X (2011).
20. G. Cao, H. Li, S. Zhan, H. Xu, Z. Liu, Z. He, and Y. Wang, "Formation and evolution mechanisms of plasmon-induced transparency in MDM waveguide with two stub resonators," *Opt. Express* **21**, 9198–9205 (2013).
21. Y. Cui and C. Zeng, "All-optical EIT-like phenomenon in plasmonic stub waveguide with ring resonator," *Opt. Commun.* **297**, 190–193 (2013).
22. Y. Bin Feng, H. Guohua, J. Cong, and C. Yiping, "Plasmon induced transparency in metal-insulator-metal waveguide by a stub coupled with F-P resonator," *Mater. Res. Express* **1**, 036201 (2014).
23. W. Yueke, W. Jicheng, L. Cheng, L. Qin, Z. Wenxiu, and G. Shumei, "Plasmonic-induced transparency in metal-dielectric-metal waveguide bends," *Appl. Phys. Express* **6**, 082201 (2013).
24. J. Liu, G. Fang, H. Zhao, Y. Zhang, and S. Liu, "Surface plasmon reflector based on serial stub structure," *Opt. Express* **17**, 20134–20139 (2009).
25. G. Veronis and S. Fan, "Bends and splitters in metal-dielectric-metal subwavelength plasmonic waveguides," *Appl. Phys. Lett.* **87**, 131102 (2005).
26. A. Mahigir, P. Dastmalchi, W. Shin, S. Fan, and G. Veronis, "Plasmonic coaxial waveguide-cavity devices," *Opt. Express* **23**, 20549–20562 (2015).
27. Z. He, H. Li, B. Li, Z. Chen, H. Xu, and M. Zheng, "Theoretical analysis of ultrahigh figure of merit sensing in plasmonic waveguides with a multimode stub," *Opt. Lett.* **41**, 5206–5209 (2016).
28. J. Shibayama, Y. Wada, J. Yamauchi, and H. Nakano, "Analysis of two- and three-dimensional plasmonic waveguide band-pass filters using the TRC-FDTD method," *IEICE Trans. Electron.* **E99-C**, 817–819 (2016).
29. E. D. Palik, *Handbook of Optical Constants of Solids* (Academic, 1997).
30. Lumerical Solutions, Inc., <http://www.lumerical.com/tcad-products/fdtd/>.
31. S. E. Kocabas, G. Veronis, D. A. B. Miller, and S. Fan, "Transmission line and equivalent circuit models for plasmonic waveguide components," *IEEE J. Sel. Top. Quantum Electron.* **14**, 1462–1472 (2008).
32. B. E. A. Saleh and M. C. Teich, *Fundamentals of Photonics* (Wiley, 2007).
33. W. Zhu, T. Xu, A. Agrawal, and H. J. Lezec, "Surface-plasmon-polariton laser based on an open-cavity Fabry–Perot resonator," arXiv:1610.03864v1 (2016).
34. J. Shibayama, H. Kawai, J. Yamauchi, and H. Nakano, "Numerical investigation of a three-dimensional stub-type plasmonic filter," in *International Conference on Numerical Simulation of Optoelectronic Devices (NUSOD)* (2016), pp. 67–68.
35. J. Shibayama, Y. Wada, J. Yamauchi, and H. Nakano, "Frequency-dependent FDTD analysis of plasmonic band-pass filters," in *IEEE 4th Asia-Pacific Conference on Antennas and Propagation (APCAP)* (2015), pp. 10–11.
36. A. Mouadili, E. H. E. Boudouti, A. Soltani, A. Talbi, B. Djafari-Rouhani, A. Akjouj, and K. Haddadi, "Electromagnetically induced absorption in detuned stub waveguides: a simple analytical and experimental model," *J. Phys.* **26**, 505901 (2014).
37. Y. Zhu, X. Hu, H. Yang, and Q. Gong, "On-chip plasmon-induced transparency based on plasmonic coupled nanocavities," *Sci. Rep.* **4**, 3752 (2014).
38. V. J. Sorger, R. F. Oulton, J. Yao, G. Bartal, and X. Zhang, "Plasmonic Fabry–Pérot nanocavity," *Nano Lett.* **9**, 3489–3493 (2009).
39. S. J. P. Kress, F. V. Antolinez, P. Richner, S. V. Jayanti, D. K. Kim, F. Prins, A. Riedinger, M. P. C. Fischer, S. Meyer, K. M. McPeak, D. Poulikakos, and D. J. Norris, "Wedge waveguides and resonators for quantum plasmonics," *Nano Lett.* **15**, 6267–6275 (2015).
40. S. Gao, Y. Wang, K. Wang, and E. Skafidas, "High contrast circular grating reflector on silicon-on-insulator platform," *Opt. Lett.* **41**, 520–523 (2016).
41. D. A. B. Miller, "Attojoule optoelectronics for low-energy information processing and communications: a tutorial review," arXiv:1609.05510 [physics.optics] (2016).
42. I. Choi and Y. Choi, "Plasmonic nanosensors: review and prospect," *IEEE J. Sel. Top. Quantum Electron.* **18**, 1110–1121 (2012).
43. G. D. Osowiecki, E. Barakat, A. Naqavi, and H. P. Herzig, "Vertically coupled plasmonic slot waveguide cavity for localized biosensing applications," *Opt. Express* **22**, 20871–20880 (2014).